surfaces

MDPI

Article

One-Step Spark Plasma Erosion Processing of Carbon-Coated Sn-Si Nanoparticles for Lithium-Ion Battery Anodes

Emma Marie Hamilton White [1,*], Lisa M. Rueschhoff [2], Takeshi Kobayashi [3], Jonathan Z. Bloh [1], Steve W. Martin [4] and Iver E. Anderson [4,5]

[1] DECHEMA Research Institute, Materials and Corrosion Division, Theodor-Heuss-Alle 25, 60486 Frankfurt am Main, Germany; jonathan.bloh@dechema.de
[2] Air Force Research Laboratory, Materials and Manufacturing Directorate, Wright-Patterson Air Force Base, OH 45433, USA; lisa.rueschhoff.1@us.af.mil
[3] Ames National Laboratory (USDOE), 229 Spedding Hall, Ames, IA 50011, USA; takeshi@ameslab.gov
[4] Department of Materials Science and Engineering, Iowa State University, 2220 Hoover Hall, Ames, IA 50011, USA; swmartin@iastate.edu (S.W.M.); andersoi@iastate.edu (I.E.A.)
[5] Ames National Laboratory (USDOE), 222 Metals Development, Ames, IA 50011, USA; andersoi@ameslab.gov
* Correspondence: emma.white@dechema.de

Abstract: High density portable energy storage is desirable owing to the energy requirements of portable electronics and electric vehicles. The Li-ion battery's high energy density could be even further improved through the utilization of alternative materials (instead of carbon) for the anode, such as Sn or Si. Nonetheless, the large volume expansion upon lithiation, up to ~300% for $Li_{22}Si_5$, causes pulverization and rapid capacity degradation during cycling. Sn also forms a $Li_{22}Sn_5$ compound with the equivalent stoichiometric Li capacity but with enhanced ductility. Nano-sized Si and Sn have demonstrated distinctive nanoscale properties, facilitating the retention of higher capacities, particularly when coated with carbon, which improves mechanical stability. To date, the methods of synthesizing coated Si, Sn, or Si-Sn alloyed nanoparticles are complicated, costly, and not readily scalable to meet the demands of cost-effective manufacturing. Spark plasma erosion in a hydrocarbon dielectric has been explored as a one-step process to produce Sn-Si alloy nanoparticles coated with a thin carbon film, offering a scalable and cost-effective processing route. The resulting Sn-Si particles exhibited a bi-modal size distribution at ~5 nm and ~500 nm and were carbon-coated, as intended, from the hydrocarbon dielectric breakdown. The spark-eroded nanoparticles were thoroughly characterized using TEM/EDS, XPS, AES, SSNMR, and TGA, and their improved electrochemical performance was assessed through half-cell experiments.

Keywords: batteries—Li-ion; nanoscale materials; silicon; spark plasma erosion; tin; carbon-coating

Citation: White, E.M.H.; Rueschhoff, L.M.; Kobayashi, T.; Bloh, J.Z.; Martin, S.W.; Anderson, I.E. One-Step Spark Plasma Erosion Processing of Carbon-Coated Sn-Si Nanoparticles for Lithium-Ion Battery Anodes. *Surfaces* **2024**, *7*, 725–738. https://doi.org/10.3390/surfaces7030047

Academic Editors: Kurt W. Kolasinski, Jaeho Kim and Susumu Yonezawa

Received: 1 July 2024
Revised: 28 August 2024
Accepted: 5 September 2024
Published: 10 September 2024

1. Introduction

Given the proliferation of portable electronics and the increasingly larger integration of electric vehicles into modern society, it is crucial that portable energy storage systems (batteries) continue to increase their energy and power densities. Li-ion batteries have the highest energy density among any commercially available portable energy storage technology [1]. If Sn (~990 mAh/g) or Si (~3500 mAh/g) were used as an anode material in Li-ion batteries instead of the currently used low-capacity carbon (~300 mAh/g), the capacity could be significantly increased [2,3]. Improved capacity by minor additions of Si and Sn to graphite anodes is already commercially applied and demonstrates the potential for these materials if they can be fully exploited [4]. To achieve this improved capacity, the large volume expansion, up to 300% for full lithiation of Si or Sn, to obtain $Li_{22}(Si/Sn)_5$ must be managed since it causes brittle failure of the material and disconnection from the current and ionic collectors in the anode [2,3,5–8].

One way to resolve this fracture resulting from volume expansion is to scale the Sn/Si particles down to the nano-level to take advantage of unique nanoscale mechanics to mitigate the pulverization of the material during charge/discharge cycling [9–11]. The theoretical critical fracture radius of Sn is 200 nm and of Si is 0.09 nm [12]. However, the experimental evidence indicates Si particles smaller than about 150 nm can circumvent mechanical fracture due to its unique nanoscale mechanical properties [9]. Moreover, coatings on such nanoparticles, especially carbon coatings, have been found to be advantageous for capacity stability [13–17]. Thin carbon coatings on such nanoparticles are essentially transparent to the alloying Li^+ ions, electronically conducting, and sufficiently strong to assist in maintaining the mechanical integrity of the Si nanoparticles [13–17]. For example, Cho et al. achieved successful cycling of nanoscale Si for up to 40 cycles at 3500 mAh/g utilizing carbon-coated 10 nm Si particles produced via a pyrolysis process [18].

The synthetic processes hitherto employed for the production of carbon-coated Si nanoparticles are costly, time-consuming, multi-stepped, and complicated to scale up for industrial mass production [18]. Recent advancements have focused on the scalability and cost of Si/Sn nanoparticles nearly as much as the capacity of Si/Sn. Sun et al. performed magnesiothermic reduction of attapulgite clay followed by polypyrrole coating to achieve scalable carbon-coated Si nanoparticles [19]. Zhu et al. used high-energy mechanical milling followed by carbonization of citric acid to produce large-scale Si and ferrosilicon carbon-coated nanoparticles [20]. These methods necessitate multiple steps, and an approach for the industrial-scale production of carbon-coated Sn/Si nanoparticles in a singular, uncomplicated step for the anodes of lithium-ion batteries is eagerly awaited.

Recently, a single-step method for an aggregated matrix of Si/Sn nanowires and nanoparticles demonstrated a reversible capacity of 580 mAh/g [21]. A commercial method to make carbon-coated Sn/Si nanoparticles in a single simple step for anodes in lithium-ion batteries would make a dramatic improvement in the battery industry. This would allow for practical commercialization of a Sn-Si nanoparticle-based anode material, replacing the typical commercial carbon anode and significantly improving the Li-ion battery capacity.

Spark plasma erosion (SPE) has been known for many years to produce nanoscale particles of various metals, including Si (which in that case was then pyrophoric when exposed to air) [22]. In SPE, two consumable electrodes are separated by a small gap, immersed in a dielectric fluid, and connected to a pulsed external power source. Upon the application of a sufficient electric field, breakdown of the dielectric fluid occurs, producing a spark discharge between the electrodes. Electrons emitted from the cathode into the gap are energized by the electric field and thereby ionize the molecules of the dielectric fluid. The resulting plasma channel (tens of microns in diameter, with temperatures in excess of 10,000 K and at pressures of about 300 MPa) transfers energy to locally heat the electrode surfaces [23]. This highly localized heating can eject vaporized and/or molten material from the electrode surfaces [24]. The ejected material, either vapor or melt, is rapidly quenched by the dielectric fluid that surrounds the channel, leading to the formation of fine, spherical particles.

Berkowitz et al. demonstrated the capability to control particle production by SPE, specifically to increase or decrease the relative quantities of the resulting particles in the bimodal distribution by promoting either the melting or evaporation modes operating at the surface of the electrodes interacting with the plasma discharge [25]. This bimodal distribution of particles is commonly observed in SPE and is caused by the melting (larger particles) or evaporation (smaller particles) modes [25]. They have also reported some interaction between the electrodes and the dielectric fluid during the spark erosion process that changed the chemistry of the resulting particles, depending on the electrode and dielectric composition [24].

In this work, the hypothesis that a carbon layer can be formed on the particles in situ during the erosion/quenching process through ionization of a hydrocarbon dielectric fluid was explored. The absence of a thick exterior oxide layer on 95Si-5at.%Sn particles in preliminary experiments suggested that the significant reaction with ambient oxygen that

Si normally exhibits had been suppressed and provided evidence indicating carbon layer formation that supports the hypothesis.

In further study of this processing route for carbon-coated alloy nanoparticles, Sn-Si alloy (Sn-rich) electrodes were used due to the poor electronic conductivity and small critical fracture radius of pure Si. A composition of 80Sn-20at.%Si was selected to create essentially metallic (high conductivity) Sn-Si electrodes to increase the particle yield from the spark plasma erosion process. The Sn content in the resulting Sn-Si nanoparticles likely also symbiotically increases the maximum usable particle size threshold since Sn has a critical fracture radius over 100 times greater than pure Si [11]. Other studies have shown that Sn improves the electrochemical behavior of Si [21,25] in addition to having high capacity on its own [8,26]. Finally, the partially metallic Sn-Si nanoparticles that resulted, with increased electronic conductivity, could provide higher rates of electron and lithium ion transfer for high-capacity anodes [15–17].

In this work, Sn-Si alloy particles resulting from spark erosion processing have been examined to explore a one-step route to preparing high-quality, high-purity Si-containing carbon-coated nanoparticles. The particles produced by spark erosion in kerosene were characterized using TEM, EDS, XPS, AES, NMR, and TGA. These nanoparticles pushed the limits of resolution of conventional materials characterization techniques due to their size, morphology, and composition, and thus the full suite of materials characterization techniques were necessary to determine the particle size, morphology, composition, and to investigate the form and location of the carbon in the sample. Finally, these carbon-coated Sn-Si alloy particles were tested in half-cells to determine their electrochemical performance and potential for use in an advanced Li-ion battery.

2. Materials and Methods

The SPE process, diagramed in Figure 1, was used to produce Sn-Si alloy particles using a Sharp Industries, Inc. (Torrance, CA, USA) 300C series electrode discharge machining (EDM) unit with a modified (low volume) erosion chamber and a rotating spindle attachment. The key parameters are listed in Table 1. Kerosene (Sigma-Aldrich, St. Louis, MO, USA, reagent grade) was used as the dielectric liquid. The electrodes were 16 mm diameter drop (chill) cast rods of 80Sn-20at.%Si produced in-house from commercial (99.9% purity) elemental materials. After sparking, the particles were centrifuged at 17,000 rpm in a Beckman Coulter (Indianapolis, IN, USA) Avanti-JE centrifuge with a JA-17 rotor. After decanting excess kerosene, the settled particles were solvent washed with hexane (Alfa-Aesar, Haverhill, MA, USA, n-Hexane HPLC grade 95+%) through five exchanges.

Transmission electron microscopy (TEM) and energy-dispersive X-ray spectroscopy (EDS) were used to characterize the resulting particles. Bright field images, diffraction patterns (SADP), and EDS of the SPE particles were obtained with a Tecnai G2 F20 TEM (FEI, Hillsboro, OR, USA) operated at 200 keV. X-ray photoelectron spectroscopy (XPS) was performed on a Perkin Elmer (Shelton, CT, USA) PHI 5500 ESCA System with a Ag filament. A JEOL (Peabody, MA, USA) JAMP-7830F field emission auger electron spectroscopy (AES) instrument was used, operating at 10 kV and 5 kV. For TEM, XPS, and AES analysis, samples (suspended in hexane) were dropped onto grids/stubs, allowed to evaporate briefly, and then inserted immediately into each instrument to minimize any interaction with ambient air.

Solid-state NMR (SSNMR) experiments utilizing ^{29}Si direct-polarization (DP) and ^{13}C{^{1}H} cross-polarization under magic-angle spinning (CP)MAS were performed at 9.4 T on a Chemagnetics (Palo Alto, CA, USA) Infinity spectrometer and at 14.1 T on a Varian (Palo Alto, CA, USA) VNMRS spectrometer, respectively. The particles were packed in a 3.2 mm MAS zirconia rotor equipped with an airtight cap including two O-rings within a glove box under a purified Ar atmosphere. The ^{13}C and ^{29}Si chemical shifts were referenced to tetramethylsilane (TMS) at 0 ppm. Additional experimental details are listed in the figure captions.

A Netzsch (Burlington, MA, USA) STA 409 PC was used for simultaneous thermogravimetric analysis (TGA) and differential scanning calorimetry (DSC). After purging the instrument chamber, the sample was heated from room temperature to 100 °C at 5 °C/min, isothermally held for 5 min. at 100 °C to remove any residual solvent, and then heated from 100 °C to 800 °C at 5 °C/min. Two runs were performed for oxidation comparison: one sample under a dry air atmosphere and the other sample under UHP (99.995%) He.

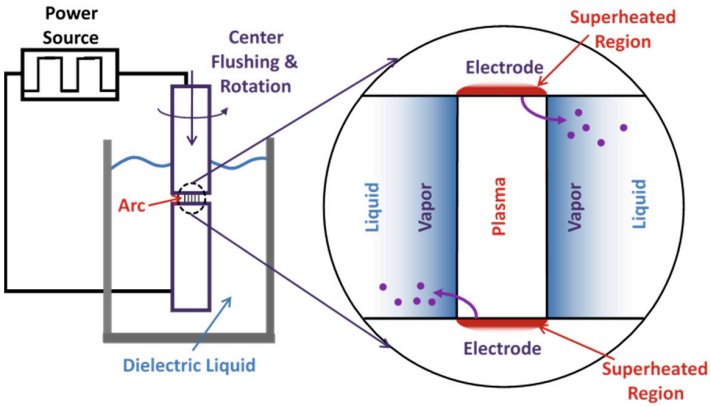

Figure 1. SPE process schematic, adapted from Berkowitz [23].

Table 1. SPE key processing parameters.

Spark Time On	2 µs
Spark Time Off	4 µs
High Voltage Current	0 A
Low Voltage Current	1.5 A
Gap Voltage	1 V
Polarity	Reverse
Rotation Speed	~130 rpm

For electrochemical testing, the SPE particles were mixed in a slurry with ratios of 10:70:5:15, 30:50:5:15, 50:30:5:15, and 70:10:5:15 by weight of SPE particles to graphite (Timrex, Paris, France, SFG 6L) to carbon black (Timrex, Super C65) to Poly(acrylic acid) (PAA, Sigma-Aldrich, Mw ~450,000). Different slurry compounding ratios for SPE particles to graphite, beginning at 10:70, were used since Beattie et al. have observed low-Si-concentration electrodes to have better cycling performance [27]. The SPE particles and carbon additives were mixed in water using an ultrasonic probe for 1 min, followed by adding PAA and stirring at 800 rpm for 1 h, and then cast on cleaned Cu foil (25 µm thick) using a doctor blade set to ~250 µm. The electrode castings were dried overnight in air, further dried in a vacuum oven at 70 °C for several hours, and then transferred immediately into a high-purity Ar atmosphere glovebox.

Half-cells of the electrodes were made in an Ar atmosphere glovebox (<10 ppm oxygen and water levels) to minimize water contamination and to prevent reaction of the Li metal and the moisture-sensitive electrolyte. A 2016 cover and can were used with the corresponding polypropylene gasket and Ni foam as a spacer and spring, respectively. The counter-electrode used was 0.38 mm thick Li metal (Sigma-Aldrich, 99.9%), punched to a 14.3 mm diameter. A separator of 25 µm thick Celgard (Charlotte, NC, USA) 2400 microporous polyethylene punched to a 19.1 mm diameter circle was used to prevent the electrodes from touching. The electrodes were punched into 7.9 mm diameter disks. The components were assembled and wetted with 30 µL of 1 M $LiPF_6$ in EC:DEC at a 1:1 ratio electrolyte.

The electrodes were charge/discharge cycled in Li metal half-cells to determine their electrochemical performance using an ARBIN (College Station, TX, USA) BT-2000 system.

The cells were cycled first at a C/20 rate based upon their theoretical capacity within a voltage range of 0.01 to 1.0 V for 2 cycles with a taper charge for formation of the solid electrolyte interface (SEI) layer. Then, using the actual charge capacity from the second cycle, the cells were cycled at a C/10 rate from 0.01–1.0 V for 200 cycles. The cycling data was analyzed to determine the coulombic efficiency of the cells, as calculated by Equation (1).

$$\%CE = 100\% - \frac{\text{discharge capacity} - \text{charge capacity}}{\text{discharge capacity}} \times 100\% \quad (1)$$

3. Results and Discussion

3.1. TEM and EDS

TEM bright field images showed the particle size distributions to be bi-modally distributed and centered at ~5 nm and ~500 nm, as seen by the representative micrographs in Figure 2. More quantitative size distribution measurements using automated nanoparticle size analysis (e.g., Sympatec Nanophox PCCS system) were frustrated by the agglomeration of the finest nanoparticles. Attempts to effectively disperse/de-agglomerate the nanoparticle size fraction were futile using standard dispersants, filters, and ultrasonication. This type of bimodal distribution agrees with the results from Berkowitz, i.e., that the smaller particles are likely produced in a mixed mode process from rapidly quenched vaporized material and larger particles from molten material ejected from the electrode surfaces due to variations in the highly localized heating from the plasma channel produced during spark erosion [23].

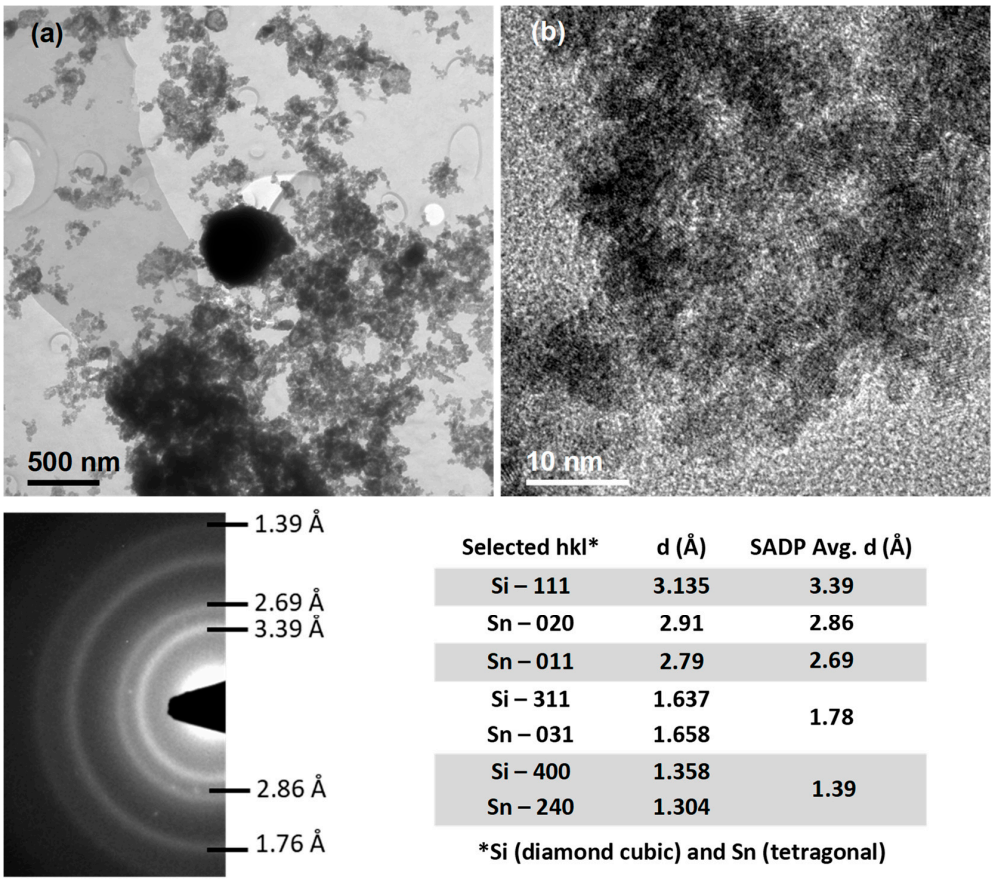

Selected hkl*	d (Å)	SADP Avg. d (Å)
Si – 111	3.135	3.39
Sn – 020	2.91	2.86
Sn – 011	2.79	2.69
Si – 311	1.637	1.78
Sn – 031	1.658	
Si – 400	1.358	1.39
Sn – 240	1.304	

*Si (diamond cubic) and Sn (tetragonal)

Figure 2. TEM of 80Sn-20at.%Si SPE particles: (**a**) Bright field image of representative bimodal distribution (one larger particle at center and agglomerated smaller particles) with indexed SADP, including indexed diffraction rings and table of results; (**b**) High-resolution image of agglomerated/overlapping smaller particles with lattice fringes.

EDS showed the presence of significant carbon in the sample, consistent with interaction with the kerosene (thermal decomposition) during spark erosion, and a variation in the Sn and Si content depending on the size of the particles. The smaller particles averaged approximately 56Sn-44at.%Si (±5at.%), while the larger were close to the initial composition of 80Sn-20at.%Si (±5at.%). In the agglomerated small particles, the apparent carbon content was as high as 85at.%, while the larger particles indicated about 20at.% carbon. Both observations of the carbon content are consistent with the large difference in the surface area to volume ratio of the two particle size modes, i.e., where the particle surface thoroughly dominates for 5 nm particles and is not nearly as prominent in 500 nm particles.

3.2. XPS

In the XPS spectra of the SPE particles, Si2p, $Sn3d_{5/2}$, C1s, and O1s peaks were evident, as shown in Figure 3. The C peak was shifted due to charging to align it with the graphite and $(CH_2)_n$ binding energies at ~284.4 and ~284.8 eV, respectively [28]. However, these two values were too close to resolve individually in this sample. Both the Sn metal (484.65 eV) and oxide (486.4 eV) peaks are evident in the Sn spectra upon etching [28]. The Si counts are low, almost at background level, and thus the form of Si is unidentifiable from this method. This is likely due to the lower amount of Si in the sample, the low sensitivity of Si, and the detection limit of Si in the presence of Sn due to the background intensity from the Sn peaks beneath the Si 2p peak.

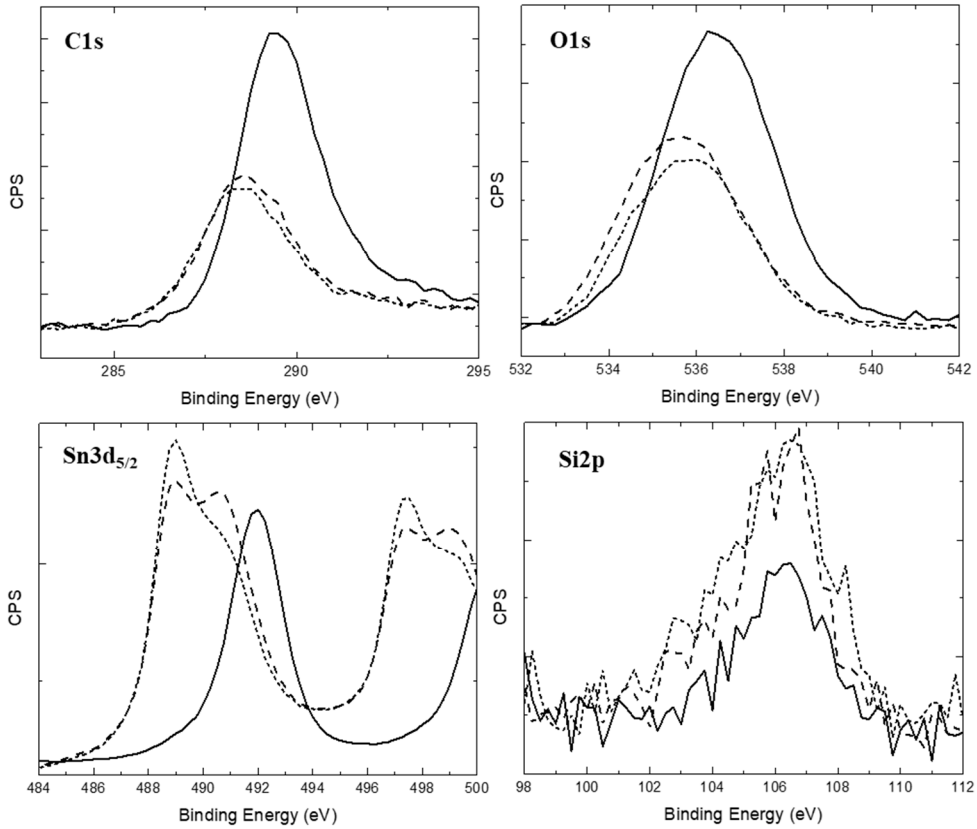

Figure 3. XPS spectra of 80Sn-20at.%Si SPE particles: C1s, O1s, $Sn3d_{5/2}$, and Si2p peaks. Solid is pre-etching, long dashed is after Ar-ion etching ~5 min, and short dashed is after a further ~5 min etch. The approximate etching rate is 10 nm/minute. All data are shown without shifting from sample charging.

The post-collection shift of the C1s peak to 284.4–284.8 eV due to charging moved the O1s, Si2p, and $Sn3d_{5/2}$ peaks to match their respective binding energies fairly closely [28]. The peak position for cubic silicon carbide is 99.5 eV for Si2p and 282.4 eV for C1s [29].

If the C1s peak is shifted to account for possible formation of SiC, the other peaks would also need to be shifted accordingly. However, this type of correction requires that the other peak positions must be shifted too far to line up well with the actual data. This result suggests that the carbon cannot be present as carbide in the nanoparticles. After performing Ar-ion etching, the tin oxide peak decreases in intensity, indicating the oxide forms after the (carbon-coated) particles form and is likely from absorbed oxygen when the sample is exposed briefly to the atmosphere during mounting and solvent washing for measurement. Both the carbon and oxygen continue to decrease with further Ar-ion etching. The Si and Sn peaks shifted to lower binding energy with etching, indicating more metallic character in the bonds towards the core of the particles. This is a strong indication that the carbon is present on the surface as a hydrocarbon and as an adhered layer on the particles.

3.3. AES

Multiple point scans with depth profiling using AES showed the sample contained O, C, Si, and Sn. The carbon content was fairly constant with depth profiling of the smaller particles, while the oxygen peak intensity was significantly reduced, as shown in Figure 4a. For the larger particles, Ar^+ etching was able to remove a large portion of the carbon and oxygen, as shown in Figure 4b. Etching occurred at an estimated rate of ~10 nm per minute.

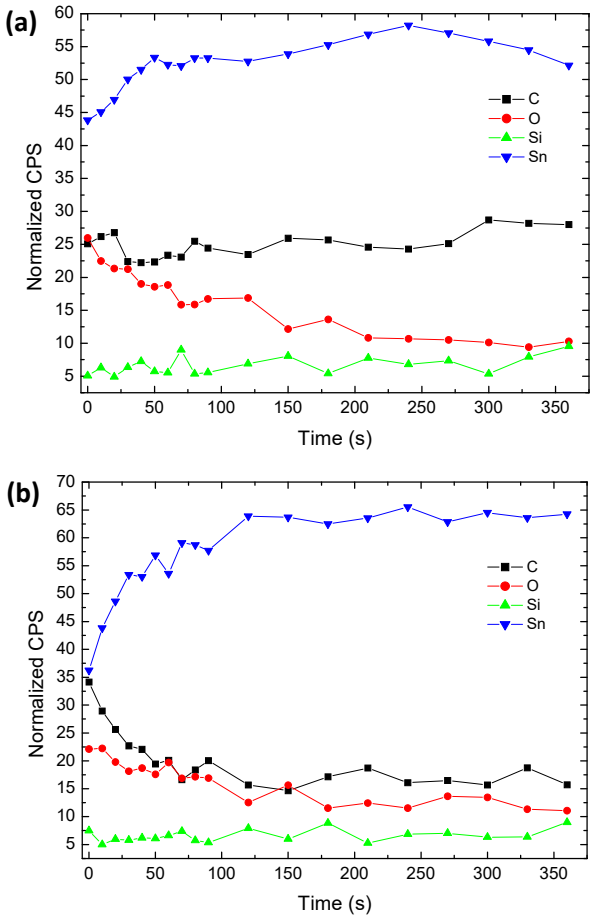

Figure 4. AES composition depth profiles: (**a**) Smaller SPE particles and (**b**) Single larger SPE particle, etching at an estimated ~10 nm/min. Points were chosen to examine the range of SPE particles present. Other sample points showed similar profiles (not included).

The larger particles, when etched, could be cleaned (fairly completely) of carbon, indicating the presence of only surface carbon and as an adhered layer. The sustained level of carbon while etching the smaller particles was consistent with etching through entire particles (~10 nm) and reaching "new" carbon-coated surfaces of additional smaller

particles below. The removal of oxygen with etching on both small and larger particles indicated it to be "advantageous" oxygen due to sample exposure to the atmosphere during mounting. The carbon layer was very tenacious, as it was not easily removed with Ar-ion etching.

3.4. NMR

The $^{13}C\{^1H\}$ CPMAS spectrum of the 80Sn-20at.%Si SPE particles exhibited two major contributions centered around 80 and 35 ppm, attributed to *sp* (alkyne) and *sp*3 (alkane) carbons, respectively (Figure 5), suggesting that the carbon layer consists of aliphatic carbons. This result is somewhat discouraging, as it was anticipated that the resulting carbon layer on the particles would exhibit a more pyrolytic (pure carbon) nature, hence rendering it graphitic. A hydrocarbon layer would be insulating to both electrons and lithium ions, suggesting that post-processing pyrolysis of the particles may be required for the highest conductivity. Note that CPMAS NMR depends on heteronuclear dipolar interactions (in this case, ^1H and ^{13}C), in which only ^{13}C nuclei that have protons in their proximity are visible. Any remaining solvent signals are then invisible since, in a liquid (or liquid-like state), the dipolar interactions average out and the CP method is ineffective.

The ^{29}Si DPMAS spectrum (Figure 6) showed a broad signal centered at −64 ppm. Notably, this resonance frequency is slightly shifted toward the lower-field side as compared to that of crystalline Si (−73 ppm) [30], which may imply that the Si becomes slightly more metallic in the Sn-Si sample. The shift is not large enough to be concluded as resulting from a Knight shift, while the T_1(spin-lattice) and T_2(spin-spin) relaxations were significantly accelerated in the sample, possibly due to conduction electrons. No oxide nor carbide signatures (e.g., from SiC) were evident in the NMR spectra [31]. These NMR results suggest that the carbon layers are physically deposited onto the Sn-Si alloy nanoparticles without chemically modifying the surfaces.

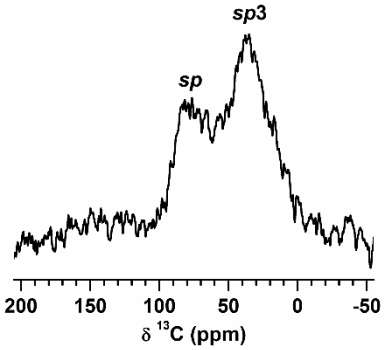

Figure 5. $^{13}C\{^1H\}$ CPMAS spectrum of 80Sn-20at.%Si SPE particles. The spectrum was taken with MAS rate ν_R = 16 kHz, recycle delay τ_{RD} = 1.5 s, number of scans NS = 8000, and acquisition time AT = 3.5 h.

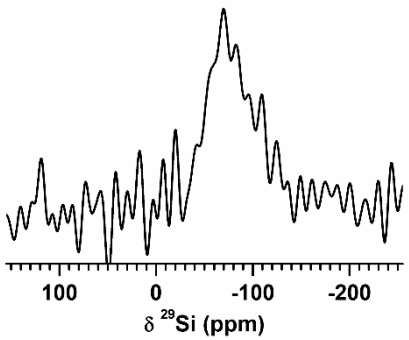

Figure 6. ^{29}Si DPMAS spectrum of 80Sn-20at.%Si SPE particles. The spectrum was taken with MAS rate ν_R = 5 kHz, recycle delay τ_{RD} = 1 s, number of scans NS = 100,000, and acquisition time AT = 28 h.

3.5. TGA

The mass (%) change with temperature from TGA of the SPE particles is shown in Figure 7. Under an inert atmosphere (He), there was less than a 5 wt.% loss up to 800 °C, while under an oxidizing atmosphere (dry air), there was less than a 3 wt.% gain in the sample mass of the 80Sn-20at.%Si particles.

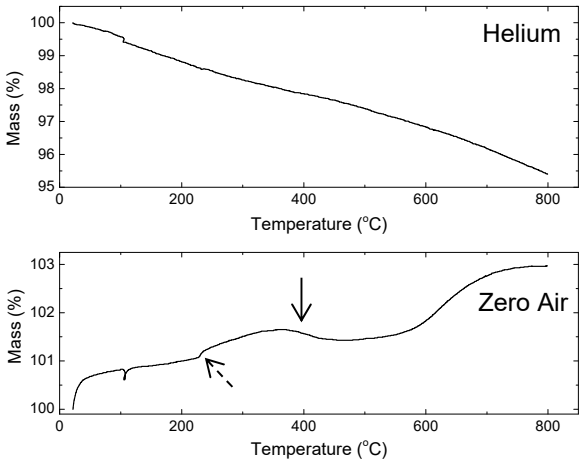

Figure 7. TGA scans of mass percent change of 80Sn-20at.%Si SPE particles under helium and dry zero air (<0.1 ppm total hydrocarbon) atmospheres. The change in slope highlighted by the dashed arrow is where Sn melts (231.93 °C) and the solid arrow points to weight loss after 400 °C.

This indicates the carbon layer on the particles is stable and conformal. The oxidation temperature ranges and temperature for maximum rate of oxidation for Si and various forms of C are shown in Table 2. From the mass (%) versus temperature of the sample under zero air, there is a change in slope (dashed arrow in Figure 7) where Sn melts (231.93 °C) and there is weight loss after 400 °C (solid arrow in Figure 7), likely the surface aliphatic carbon being volatilized. There is no change in slope that matches the possible distinct identifiable forms of carbon as listed in Table 2. There is some oxidation of the Si after 600 °C, as indicated by the weight gain in that regime. This is further evidence that the carbon is not present as SiC on the surface of the particles, since SiC is extremely stable past 800 °C in air and, if present, would prevent any oxidation of the particles in this temperature range.

Table 2. Oxidation behavior of various materials in air.

Material	Oxidation Temperature (°C)	Ref.
Si	>300 °C (slow) >600 °C (rapid)	[32]
amorphous C	250 °C	[33]
C nanotubes/nanoparticles	695 °C	[34]
C_{60}	420 °C	[34]
graphite	645 °C	[34]
diamond-like coating	500 °C	[35]
soot	585 °C	[36]
alkyl groups on Si nanoparticles	518 °C	[37]
SiC nanoparticles	over 800 °C	[38]

3.6. Other Particle Observations

Other observations also support the apparent decomposition of the kerosene to form a carbonaceous layer on the particles during SPE. There is a significant color difference between Sn-Si nanoparticles produced in kerosene versus nanoparticles produced in water for reference (Figure 8). The kerosene SPE particles are dark black, while the water SPE particles are a light brown. The particles are in the same size range (from TEM analysis), thus the color is an indication of surface character. Si nanoparticles produced in a water dielectric, thus likely having an oxidized surface due to interaction with the dielectric and the availability of oxygen, appear very similar to purchased oxidized Si nanoparticles.

Figure 8. Samples of SPE and purchased powders: (**a**) 98.8Si-1.2at.%Sn from kerosene SPE; (**b**) 80Sn-20at.%Si from kerosene SPE; (**c**) 98.8Si-1.2at.%Sn from water SPE; and (**d**) purchased nano-Si. Particles in (**a**,**b**) are still in the kerosene dielectric, and (**c**) is still in the water dielectric fluid.

From these results, it appears that the SPE method was able to achieve the desired outcome of applying a carbonaceous (protective) surface film on Sn-Si nanoparticles. XPS and SSNMR conclusively demonstrated the lack of carbide formation, while AES and TGA gave evidence that the carbon layer is stable and conformal. The SSNMR results, indicating aliphatic carbon rather than graphitic carbon, raised some concern about the form of the carbon layer since an aliphatic C layer is not as desirable for electron and Li-ion conduction.

3.7. Electrochemical Testing

The resulting particles were tested electrochemically to determine if the C-coated Sn-Si alloy nanoparticles have increased capacity and improved reversibility as a lithium-ion battery anode material. Figure 9 shows the results of three Sn-Si alloy composite anodes with differing ratios (SPE particles:graphite:carbon black:PAA) in the electrode components. These results are compared to a graphite anode formed using the same procedure. The theoretical total electrode capacities were calculated to be 460 mAh/g for the 10:70:5:15, 640 mAh/g for the 30:50:5:15, and 820 mAh/g for the 50:30:5:15 ratio electrodes, where both the SPE particles and graphite were considered together as the active material.

Figure 9 demonstrates the 80Sn-20at.%Si particles, when added in a 10:70:5:15 ratio electrode, began at a capacity of ~350 mAh/g and gradually decreased to ~320 mAh/g after 175 cycles. This is relatively close to the theoretical capacity of 460 mAh/g for the 10:70:5:15 electrode and is higher than currently used commercial carbon (typically <300 mAh/g) [39,40]. The other higher active material ratio electrodes had higher initial capacities (close to their theoretical values) but greater capacity fade. This agrees with Beattie et al. [27], where higher binder contents accommodated the large volume expansion better and reduced the capacity fade of Si composite anodes. Although other processing methods have demonstrated higher capacities, e.g., ~2000 mAh/g [13], 1450 mAh/g [14], or 1200–1360 mAh/g [20], for these types of Si- and Sn- nanowire and nanoparticle materials, these methods are costly and complex and typically require upwards of 80 wt.% of active (expensive) material to achieve these capacities. Other more scalable methods are in the range of 400–700 mAh/g [15–17,21], similar to the results here, but again utilize up to 100% active material, the most expensive component. The most stable and greatest increase in capacity here utilized only 10% of the SPE particles, demonstrating the high potential of a small quantity of these SPE particles to significantly increase today's battery capacities.

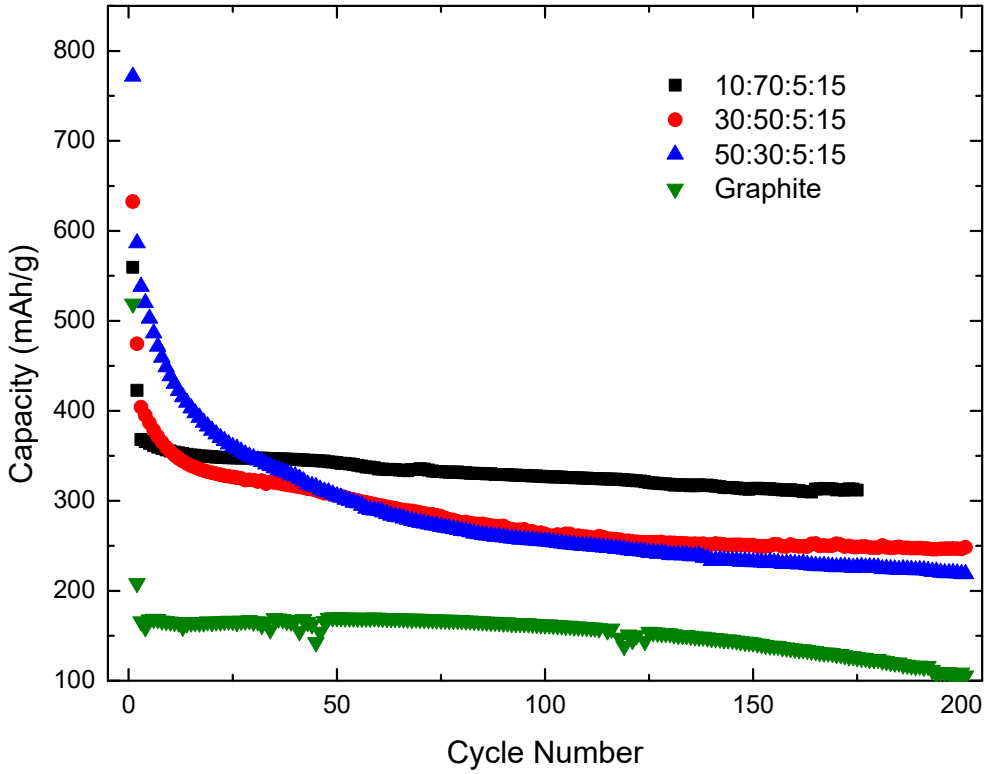

Figure 9. Capacity vs. cycle number for 80Sn-20at.%Si SPE particles for differing ratios of active material. Included for comparison is a graphite half-cell (80:5:15 ratio).

The lower than theoretical capacity of the 80Sn-20at.%Si could be due to the large amount of aliphatic carbon present on the particles, which would have low conductivity and capacity for Li. Also, decomposition of this layer and interaction with the liquid electrolyte would further limit the capacity of the particles. With more SPE particles in the electrode, the amount of hydrocarbon would be greater, thus the conductivity could be lowered, along with capacity. Further optimization of the process with differing parameters and modified electrode and dielectric chemistries to promote more complete hydrocarbon dissociation would be beneficial to the overall performance of these materials.

The lower than expected reversible capacity can also be partially attributed to the bimodal distribution of spark-eroded particles in the anode layer that still includes particles larger than the ~150 nm experimental critical particle size for Si [9] and near the ~200 nm theoretical critical size for Sn [12]. These larger particles of the bimodal distribution are likely fracturing during cycling and losing electrical conductivity, thus causing capacity to fade during cycling. Additionally, fresh fracture surfaces will form a new SEI layer, further reducing the capacity of the cells. Again, increasing the amount of SPE particles adds additional larger-than-critical-size particles, which will decrease the performance and capacity of the electrode. Attempts to separate the larger size (micron-scale) fraction from the nano-fraction have so far been unsuccessful. Development of new SPE geometries and technologies could enable better process control and thus particle size control for production of particles under ~150 nm.

Future work will focus on de-aggregating the nanoparticles and developing an effective mechanism to select only the nano-metric fraction of particles to provide anode material with particles consistently below the critical fracture radius. Additionally, future work will include pyrolysis of the hydrocarbon surface layer to graphitic carbon to investigate the possibility of achieving higher conductivity and/or capacity in the currently available C-coated Sn-Si nanoparticles.

4. Conclusions

SPE of 80Sn-20at.%Si electrodes in kerosene successfully produced C-coated Sn-Si nanoparticles in a bimodal size range distributed at ~5 nm and ~500 nm in a single processing step. The carbon is present as an adhered, tenacious layer on the particles that is comprised primarily of hydrocarbon species. The SPE C-coated Sn-Si alloy nanoparticles exhibited a reversible capacity of ~350 mAh/g, which is higher than the average graphite anode that practically attains only ~300 mAh/g. This level of battery performance was reached in spite of the partially decomposed hydrocarbon (aliphatic C) surface layer on the anode particulate, which can be insulating to both electrons and lithium ions, likely limiting the overall capacity and reversibility of these particles. Thus, these new, scalable Sn-Si anode materials have high potential to increase Li-ion battery capacity, especially with further optimization.

Author Contributions: Conceptualization, E.M.H.W., S.W.M. and I.E.A.; Data curation, E.M.H.W., T.K. and L.M.R.; Formal analysis, E.M.H.W. and T.K.; Funding acquisition, E.M.H.W., S.W.M. and I.E.A.; Investigation, E.M.H.W., L.M.R. and T.K.; Methodology, E.M.H.W., L.M.R., T.K., S.W.M. and I.E.A.; Project administration, S.W.M. and I.E.A.; Resources, E.M.H.W., S.W.M. and I.E.A.; Supervision, J.Z.B., S.W.M. and I.E.A.; Validation, E.M.H.W., L.M.R., T.K., S.W.M. and I.E.A.; Writing—original draft, E.M.H.W. and T.K.; Writing—review & editing, E.M.H.W., L.M.R., T.K., J.Z.B., S.W.M. and I.E.A. All authors have read and agreed to the published version of the manuscript.

Funding: E.W. was supported by a graduate fellowship received from the NASA Aeronautics Scholarship Program and a subsequent fellowship through the NSF GK-12 Symbi program while at Iowa State University. Spark plasma erosion processing research, supervised by I.A., was supported by the Ames Lab Seed Fund and by the U.S. Department of Energy, Office of Basic Energy Sciences, Division of Materials Sciences and Engineering. Ames National Laboratory is operated for DoE by Iowa State University under Contract DE-AC02-07CH11358. The half-cell testing, supervised by S.M., was supported by the NSF through grant numbers DMR 0710564 and DMR 1304977 and the DOE-Sandia National Laboratory-Arizona State University through contract number 11080469.

Institutional Review Board Statement: Not Applicable.

Informed Consent Statement: Not Applicable.

Data Availability Statement: The data is available upon request from the corresponding author.

Acknowledgments: The authors thank Jim Anderegg at Ames National Laboratory for XPS and AES examination of the nanoparticles.

Conflicts of Interest: The authors declare no conflict of interest.

References

1. Tarascon, J.M.; Armand, M. Issues and challenges facing rechargeable lithium batteries. *Nature* **2001**, *414*, 359–367. [CrossRef] [PubMed]
2. Kasavajjula, U.; Wang, C.; Appleby, A.J. Nano- and bulk-silicon-based insertion anodes for lithium-ion secondary cells. *J. Power Sources* **2007**, *163*, 1003–1039. [CrossRef]
3. Winter, M.; Besenhard, J.O. Electrochemical lithiation of tin and tin-based intermetallics and composites. *Electrochim. Acta* **1999**, *45*, 31–50. [CrossRef]
4. Blomgren, G.E. The Development and Future of Lithium Ion Batteries. *J Electrochem. Soc.* **2017**, *164*, A5019. [CrossRef]
5. Winter, M.; Besenhard, J.O.; Spahr, M.E.; Novak, P. Insertion electrode materials for rechargeable lithium batteries. *Adv. Mater.* **1998**, *10*, 725–763. [CrossRef]
6. Yang, J.; Winter, M.; Besenhard, J.O. Small particle size multiphase Li-alloy anodes for lithium-ion-batteries. *Solid State Ionics* **1996**, *90*, 281–287. [CrossRef]
7. Bourderau, S.; Brousse, T.; Schleich, D.M. Amorphous silicon as a possible anode material for Li-ion batteries. *J. Power Sources* **1999**, *81*, 233–236. [CrossRef]
8. Li, W.; Sun, S.; Yu, Y. Ge- Si-, Sn-based anode materials for lithium-ion batteries: From structure design to electrochemical performance. *Small Methods* **2017**, *1*, 1600037. [CrossRef]
9. Liu, X.H.; Zhong, L.; Huang, S.; Mao, S.X.; Zhu, T.; Huang, J.Y. Size dependent fracture of silicon nanoparticles during lithiation. *ACS Nano* **2012**, *6*, 1522–1531. [CrossRef]

10. Graetz, J.; Ahn, C.C.; Yazami, R.; Fultz, B. Highly reversible lithium storage in nanostructured silicon. *Electrochem. Solid-State Lett.* **2003**, *6*, A194–A197. [CrossRef]
11. Lee, K.T.; Cho, J. Roles of nanosize in lithium reactive nanomaterials for lithium ion batteries. *Nano Today* **2011**, *6*, 28–41. [CrossRef]
12. Huggins, R.A.; Nix, W.D. Decrepitation model for capacity loss during cycling of alloys in rechargeable electrochemical systems. *Ionics* **2000**, *6*, 57–63. [CrossRef]
13. Kwon, Y.; Cho, J. High capacity carbon-coated Si70Sn30 nanoalloys for lithium battery anode material. *Chem. Commun.* **2008**, 1109–1111. [CrossRef]
14. Wang, G.X.; Ahn, J.H.; Yao, J.; Bewlay, S.; Liu, H.K. Nanostructured Si-C composite anodes for lithium-ion batteries. *Electrochem. Commun.* **2004**, *6*, 689–692. [CrossRef]
15. Elia, G.A.; Panero, S.; Savoini, A.; Scrosati, B.; Hassoun, J. Mechanically milled, nanostructured Sn-C composite anode for lithium ion battery. *Electrochim. Acta* **2013**, *90*, 690–694. [CrossRef]
16. Xu, Y.; Liu, Q.; Zhu, Y.; Liu, Y.; Langrock, A.; Zachariah, M.R.; Wang, C. Uniform nano-Sn/C composite anodes for lithium ion batteries. *Nano Lett.* **2013**, *13*, 470–474. [CrossRef]
17. Zhou, X.; Zou, Y.; Yang, J. Carbon supported tin-based nanocomposites as anodes for Li-ion batteries. *J. Solid State Chem.* **2013**, *198*, 231–237. [CrossRef]
18. Kim, H.; Seo, M.; Park, M.-H.; Cho, J. A critical size of silicon nano-anodes for lithium rechargeable batteries. *Angew. Chem. Int. Ed.* **2010**, *49*, 2146–2149. [CrossRef]
19. Sun, L.; Su, T.; Xu, L.; Du, H.-B. Preparation of uniform Si nanoparticles for high-performance Li-ion battery anodes. *Phys. Chem. Chem. Phys.* **2016**, *18*, 1521. [CrossRef]
20. Zhu, B.; Jin, Y.; Tan, Y.; Zong, L.; Hu, Y.; Chen, L.; Chen, Y.; Zhang, Q.; Zhu, J. Scalable Production of Si Nanoparticles Directly from Low Grade Sources for Lithium-Ion Battery Anode. *Nano Lett.* **2015**, *15*, 5750–5754. [CrossRef]
21. Uchida, G.; Masumoto, K.; Sakakibara, M.; Ikebe, Y.; Ono, S.; Koga, K.; Kozawa, T. Single-step fabrication of fibrous Si/Sn composite nanowire anodes by high-pressure He plasma sputtering for high-capacity Li-ion batteries. *Nat. Sci. Rep.* **2023**, *13*, 14280. [CrossRef] [PubMed]
22. Vons, V.A.; de Smet, L.C.P.M.; Munao, D.; Evirgen, A.; Kelder, E.M.; Schmidt-Ott, A. Silicon nanoparticles produced by spark discharge. *J. Nanoparticle Res.* **2011**, *13*, 4867–4879. [CrossRef]
23. Berkowitz, A.E.; Walter, J.L. Spark erosion: A method for producing rapidly quenched fine powders. *J. Mater. Res.* **1987**, *2*, 277–288. [CrossRef]
24. Hsu, M.S.; Meyers, M.A.; Berkowitz, A. Synthesis of nanocrystalline titanium carbide by spark erosion. *Scr. Metall. Mater.* **1995**, *32*, 805–808. [CrossRef]
25. Dong, Z.; Du, W.; Yan, C.; Zhang, C.; Chen, G.; Chen, J.; Sun, W.; Jiang, Y.; Liu, Y.; Gao, M.; et al. A Novel Tin-Bonded Silicon Anode for Lithium-Ion Batteries. *ACS Appl. Mater. Interfaces* **2021**, *13*, 45578–45588. [CrossRef]
26. Wu, C.; Zhu, G.; Wang, Q.; Wu, M.; Zhang, H. Sn-based nanomaterials: From composition and structural design to their electrochemical performances for Li- and Na-ion batteries. *Energy Storage Mat.* **2021**, *43*, 430–462. [CrossRef]
27. Beattie, S.D.; Larcher, D.; Morcrette, M.; Simon, B.; Tarascon, J.-M. Si electrodes for Li-ion batteries – A new way to look at an old problem. *J. Electrochem. Soc.* **2008**, *155*, A158–A168. [CrossRef]
28. Wagner, C.D.; Riggs, W.M.; Davis, L.E.; Moulder, J.F.; Mullenberg, G.E. *Handbook of X-ray Photoelectron Spectroscopy*; Perkin-Elmer Corporation: Eden Prairie, MN, USA, 1979.
29. Tabata, A.; Fujil, S.; Suzuoki, Y.; Mizutani, T.; Ieda, M. X-ray photoelectron spectroscopy (XPS) of hydrogenated amorphous silicon carbide (a-SixC1-x:H) prepared by the plasma CVD method. *J. Phys. D Appl. Phys.* **1990**, *23*, 316–320. [CrossRef]
30. Faulker, R.A.; DiVerdi, J.A.; Yang, Y.; Kobayashi, T.; Maciel, G.E. The surface of nanoparticle silicon as studied by solid-state NMR. *Materials* **2013**, *6*, 18–46. [CrossRef]
31. Hong, J.; Cho, K.-Y.; Shin, D.-G.; Kim, J.-I.; Oh, S.-T.; Riu, D.-H. Low-temperature chemical vapour curing using iodine for fabrication of continuous silicon carbide fibres from low-molecular-weight polycarbosilane. *J. Mater. Chem. A* **2014**, *2*, 2781–2793. [CrossRef]
32. Zhou, X.; Yin, Y.-X.; Wan, L.-J.; Guo, Y.-G. Facile synthesis of silicon nanoparticles inserted in graphene sheets and improved anode materials for lithium-ion batteries. *Chem. Commun.* **2012**, *48*, 2198–2200. [CrossRef] [PubMed]
33. Ng, S.H.; Wang, J.; Wexler, D.; Chew, S.Y.; Liu, H.K. Amorphous carbon-coated silicon nanocomposites: A low-temperature synthesis via spray pyrolysis and their application as high-capacity anodes for lithium-ion batteries. *J. Phys. Chem. C* **2007**, *111*, 11131–11138. [CrossRef]
34. Pang, L.S.K.; Saxby, J.D.; Chatfield, S.P. Thermogravimetric analysis of carbon nanotubes and nanoparticles. *J. Phys. Chem. Lett.* **1993**, *97*, 6941–6942. [CrossRef]
35. Ni, W.; Cheng, Y.-T.; Weiner, A.M.; Perry, T.A. Tribological behavior of diamond-like-carbon (DLC) coatings against aluminum alloys at elevated temperatures. *Surf. Coat. Tech.* **2006**, *201*, 3229–3234. [CrossRef]
36. Bredin, A.; Larcher, A.V.; Mullins, B.J. Thermogravimetric analysis of carbon black and engine soot – towards a more robust oil analysis method. *Trib. Intl.* **2011**, *44*, 1642–1650. [CrossRef]
37. Verdoni, L.P.; Fink, M.J.; Mitchell, B.S. A fractionation process of mechanochemically synthesized blue-green luminescent alkyl-passivated silicon nanoparticles. *Chem. Eng. J.* **2011**, *172*, 591–600. [CrossRef]

38. Kisku, S.K.; Dash, S.; Swain, S.K. Dispersion of SiC nanoparticles in cellulose for study of tensile, thermal and oxygen barrier properties. *Carb. Polym.* **2014**, *99*, 306–310. [CrossRef]
39. Basu, S. Ambient Temperature Rechargeable Battery. U.S. Patent 4423125, 27 December 1983.
40. Tran, T.D.; Feikert, J.H.; Song, X.; Kinoshita, K. Rate effect on lithium-ion graphite electrode performance. *J. Electrochem. Soc.* **1995**, *142*, 3297–3302. [CrossRef]